Application of Spectral Methods to Representative Data Sets in Electrophysiology and Functional Neuroimaging

David Kleinfeld, PhD

Department of Physics and Graduate Program in Neurosciences
University of California
La Jolla, California

NOTES

Background

Experimental neuroscience involves the use of many different tools from physics, genetics, and other fields. Proper data analysis is an integral part of this set of tools. Used correctly, analysis will help to define the magnitude and significance of a given neural effect; used creatively, analysis can help reveal new phenomena.

In this chapter, we consider five example cases that introduce the utility and implementation of spectral methods:

(1) Deduction of variation in the power of a high-frequency cortical oscillation from a human electrocorticogram (ECoG). This will illustrate frequency-domain concepts such as the spectrogram.
(2) Deduction of synaptic connectivity between neurons in the leech swim network. This will emphasize notions of spectral coherence and its associated confidence level.
(3) The discovery of neurons in rat vibrissa motor cortex that report the pitch of vibrissa movement. This will illustrate the notion of the spectral power density as the sum of δ-functions corresponding to pure tones and a slowly varying, or pink, spectrum.
(4) The denoising of imaging data in the study of calcium waves. This will introduce the concept of singular value decomposition (SVD) in the time domain and illustrate the notion of space-time correlation in multisite measurements.
(5) The delineation of wave phenomena in turtle cortex. This will illustrate the concept of SVD in the frequency domain and further illustrate the notion of space-time coherence.

Throughout this discussion the emphasis will be on explaining the analysis and not on the scientific questions per se.

Advantages of Working in the Frequency Domain

Why work in the frequency domain? One part of the answer is to delineate the number of degrees of freedom required to calculate confidence intervals. The following factors are relevant:

- Determining the number of degrees of freedom is complicated in the time domain, where all but white noise processes lead to correlation between neighboring data points.

- In contrast, counting the number of degrees of freedom is straightforward when neighboring data points are uncorrelated. This occurs in the frequency domain when the amplitude of spectral power in the data varies only slowly on the scale of the bandwidth, so that neighboring points in frequency are uncorrelated.

A second part of the answer is that some phenomena have a simpler representation in the frequency domain rather than the time domain.

This chapter builds on the discussion of the time-bandwidth product and multitaper analysis (Thomson, 1982) in Spectral Analysis for Neural Signals, presented earlier in this Short Course by Bijan Pesaran. First, we recall the time-frequency uncertainty:

$$T\Delta f = 2p$$

where T is the total length of the time series of the data; $2p$ is the number of degrees of freedom and defines the time-frequency product, with $p \geq 1$; and Δf is the resultant full bandwidth. The power is concentrated in the frequency interval Δf, optimally so for the use of family of Slepian tapers employed to estimate spectra (Thomson, 1982). The *maximum* number of tapers, denoted K, that supports this concentration, and which is employed throughout our presentation, is as follows:

$$K = 2p - 1.$$

Rosetta Stone

The variables used in the Pesaran chapter herein and past reviews (Mitra and Pesaran, 1998; Mitra et al., 1999) expressed in discrete, normalized variables by writing (1) $T = N\Delta t$, where N is the number of data points in the time series and $\Delta t = 1/(2f_{Nyquist})$ is the sample time; and (2) $2W = \Delta t\, \Delta f$, where W is the half-bandwidth. Thus, $NW = p$. In normalized variables, time spans the interval $[1, N]$ rather than $[\Delta t, T]$; frequency spans the interval $[-½, ½]$ rather than $[-f_{Nyquist}, f_{Nyquist}]$; and the integral

$$\frac{1}{\sqrt{T}}\int_0^T dt$$ is replaced by $$\frac{1}{\sqrt{N}}\sum_0^N$$ with $\Delta t = 1$. Tools for the numerical calculations used in the examples below are part of the Matlab-based Chronux package (www.chronux.org). The primary textbooks include those by Percival and Walden, 1993, and Mitra and Bokil, 2008.

Case one

We analyze a trace of human ECoG data, defined as $V(t)$, that was obtained in a study on ultra-slow brain activity (Nir et al., 2008) (Fig. 1A). The mean value is removed to form the following:

$$\delta V(t) = V(t) - \frac{1}{T}\int_0^T dt\, V(t).$$

NOTES

Our goal is to understand the spectral content of this signal—with confidence limits! The Fourier transform of this signal, with respect to the *k*th taper, is as follows:

$$\delta\tilde{V}^{(k)}(f) = \frac{1}{\sqrt{T}}\int_0^T dt\; e^{-i2\pi f t} w^{(k)}(t)\; \delta V(t)$$

where $w^{(k)}(t)$ is the *k*th Slepian taper, whose length is also *T*. We then compute the spectral power density, whose units are amplitude^2/Hz, in terms of an average over tapers:

$$S(f) \equiv \frac{1}{K}\sum_{k=1}^{K}\left|\delta\tilde{V}^{(k)}(f)\right|^2$$

where $\left|\delta\tilde{V}^{(k)}(f)\right|^2 = \delta\tilde{V}^{(k)}(f)\left[\delta\tilde{V}^{(k)}(f)\right]^*$; we further average the results over all trials, if appropriate. The above normalization satisfies Parseval's theorem, i.e.,

$$\int_0^{f_{Nyquist}} df\, S(f) = \frac{1}{T}\int_0^T dt\, \left[\delta V(t)\right]^2.$$

The spectrum in this example is featureless, having a hint of extra power between 50 Hz and 100 Hz (Fig. 1*B*). One possibility is that the spectrum is better defined on a short time scale, but drifts (Fig. 1*B*, insert). In this case, it is useful to compute the running spectrum, or spectrogram, denoted $S(f; t)$, which is a function of both frequency and time. Here we choose a narrow interval of time, compute the spectrum over that interval, and then step forward in time and recalculate the spectrum. For the example data, this process reveals an underlying modulation in the power between 40 Hz and 90 Hz (Fig. 1*C*): the so-called γ-band.

How do we characterize the γ-band's variations in power? We treat the logarithm of the power in a band as a new signal found by integrating the spectrogram over the frequency:

$$V_\gamma(t) \equiv \frac{1}{f_2 - f_1}\int_{f_1}^{f_2} df\; ln\left\{S(f; t)\right\}$$

This gives us a new time series (Fig. 1*D*). We take the logarithm because the spectrum is χ^2– as opposed to Gaussian-distributed; this transform stabilizes the estimate of the variance. The spectral components of the new time series are called the "second spectrum," denoted $S_\gamma(f)$ for this example:

$$S_\gamma^{(n)}(f) \equiv \frac{1}{K\text{-}1}\sum_{\substack{k=1\\k\neq n}}^{K}\left|\tilde{V}_\gamma^{(k)}(f)\right|^2 \quad \forall\; n$$

The above formula shows a number of spectral features (Fig. 1*E*) and raises two general issues.

The first issue is the calculation of confidence intervals. For variables with a Gaussian dependence on their individual spectral amplitudes, the confidence limits may be estimated in various asymptotic limits. However, the confidence intervals may also be estimated directly by a jackknife (Thomson and Chave, 1991), where we compute the standard error in terms of "delete-one" means. In this procedure, we calculate *K* different mean spectra, in which one term is left out:

$$S_\gamma^{(n)}(f) \equiv \frac{1}{K\text{-}1}\sum_{\substack{k=1\\k\neq n}}^{K}\left|\tilde{V}_\gamma^{(k)}(f)\right|^2 \quad \forall\; n$$

Estimating the standard error of $S_\gamma(f)$ requires an extra step since spectral amplitudes are defined on the interval [0, ∞) while Gaussian variables exist on (–∞, ∞). The delete-one estimates, $|C_i^{(n)}(f)|$, were replaced with the following transformed values:

$$g\left\{S(f)\right\} = ln[S(f)]$$

or

$$S(f) = e^{g\{S(f)\}}.$$

The mean of the transformed variable is as follows:

$$\mu_\gamma(f) = \frac{1}{K}\sum_{n=1}^{K} g\left\{S_\gamma^{(n)}(f)\right\}$$

and standard error of the transformed variable is as follows:

$$\sigma_\gamma(f) = \sqrt{\frac{K-1}{K}\sum_{n=1}^{K}\left|g\left\{S_\gamma^{(n)}(f)\right\} - \mu_\gamma(f)\right|^2}.$$

The 95% confidence interval for the spectral power is thus $\left[e^{\mu_{i,Mag} - 2\sigma_{i,Mag}}, e^{\mu_{i,Mag} + 2\sigma_{i,Mag}}\right]$. The confidence

NOTES

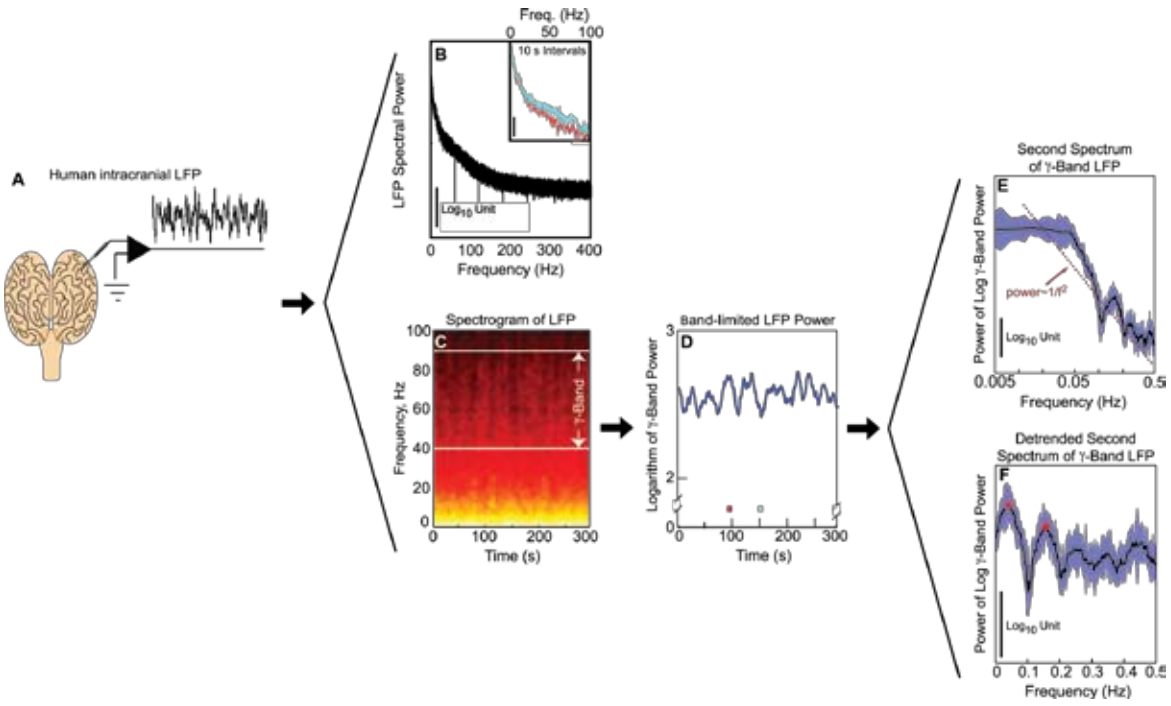

Figure 1. Analysis of the spectral properties of human local field potential (LFP) data (Drew et al., 2008, their Fig. 1, reprinted with permission from ***Nature Neuroscience***). ***A***, The LFP was obtained during stage 2 sleep; $f_{Nyquist}$ = 500 Hz. ***B***, Spectrum (***T*** = 300 s; ***K*** = 29) of the LFP in panel ***A***; insert shows spectra (***T*** = 10 s; ***K*** = 9) for the intervals demarcated in panel *D*. ***C***, Spectrogram (window ***T*** = 10 s, overlap = 1 s; ***K*** = 13) of the LFP with full bandwidth ΔF = 1.4 Hz; color scale maps the logarithm of power from black/red (low) to white/yellow (high). Note the systematic variation in power in the γ band. ***D***, Time series of the logarithm of the power in the γ band of the LFP, integrated from f_1 = 40 Hz to f_2 = 90 Hz; $f_{Nyquist}$ = 0.5 Hz. ***E***, Second spectrum (*T* = 300 s; ***K*** = 13) using the time series in panel *D* with ΔF = 0.05 Hz; blue stripe is the 95% (2σ) confidence interval. ***F***, Second spectrum using the derivative of the time series in panel *D* as a means of removing a $1/f^2$ trend.

bands are symmetric about the mean when spectral power is plotted on a logarithmic scale (Fig. 1*E*).

A second issue is a $1/f^2$ trend in the spectrum, which obscures peaks. We remove this trend by computing the spectrum of $dV_\gamma(t)/dt$ in order to reveal peaks, particularly at f = 0.05 Hz (Fig. 1*F*). The conclusion is that power in the γ-band shows slow periodic variation, which is of interest in light of the conjecture that this variation may drive spectrally similar variations in the blood oxygenation level-dependent (BOLD) functional magnetic resonance (fMR) signal (Nir et al., 2008).

Case two

We now consider the use of optical imaging to determine potential pairwise interactions between neurons (Cacciatore et al., 1999). We focus on imaging data taken from the ventral surface of a leech ganglion and seek to identify cells in the ganglion that receive monosynaptic input from neuron Tr2 in the head (Fig. 2*A*). This cell functions as a toggle for regulating the swim rhythm in these animals. Rather than serially impaling each of the roughly 400 cells in the ganglion and looking for postsynaptic currents induced by driving Tr2, a parallel strategy was adopted by Taylor and colleagues (2003). The cells in the ganglion were stained with a voltage-sensitive dye (Fig. 2*B*), which transforms changes in membrane potential into changes in the intensity of fluorescent light. The emitted light from all cells was then detected with a CCD camera (Fig. 2*B*) from which time series for the change in fluorescence were calculated for each neuron in the field. Presynaptic cell Tr2 was stimulated with a periodic signal, at frequency f_{Drive}, with the assumption that candidate postsynaptic followers of Tr2 would fire with the same periodicity (Fig. 2*C*). The phase of the coherence relative to the drive depends on several factors: the sign of the synapse, propagation delays, and filtering by postsynaptic processes.

The coherence between the response of each cell and the drive (a complex function denoted $C_i(f)$) was calculated over the time period of the stimulus. We denoted the time series of the optical signals as $V_i(t)$

NOTES

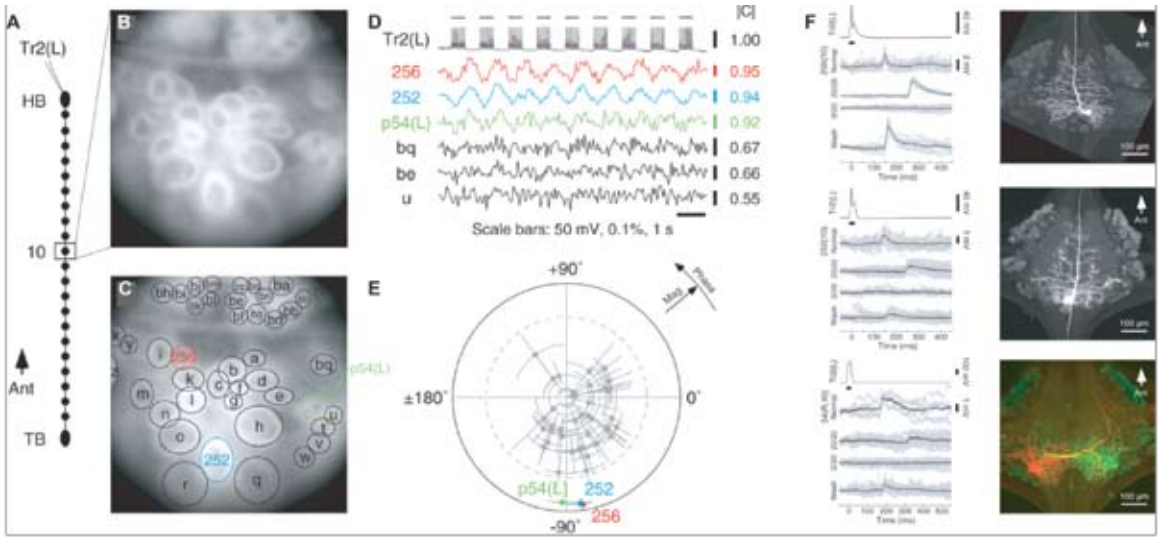

Figure 2. Analysis of voltage-sensitive dye imaging experiments to find followers of Tr2 (Taylor et al., 2003, their Fig. 1 and Fig. 3, reprinted with permission from the *Journal of Neuroscience*). ***A***, Cartoon of the leech nerve cord; input to Tr2 forms the drive ***U(t)***. ***B***, Fluorescence image of ganglion 10 stained with dye. ***C***, Ellipses drawn to encompass individual cells and define regions whose pixel outputs were averaged to form the $V_i(t)$. ***D***, Simultaneous electrical recording of Tr2, i.e., ***U(t),*** and optical recordings from 6 of the cells shown in panel ***C***, i.e., $V_1(t)$ through $V_6(t)$, along with $|C_i(f_{Drive})|$ (T = 9 s; K = 11) ***E***, Polar plot of $C_i(f_{Drive})$ between each optical recording and the cell Tr2 electrical recording for all 43 cells in panel ***C***. The dashed line indicates that $\alpha = 0.001$ is the threshold for significance; error bars = one standard error. ***F***, Results of electrophysiological tests of monosynaptic drive for cells 356, 252, and p54, along with confocal images of fills of these cells. Spike-triggered averages, each from a different condition, are shown with error bands. The spike in Tr2 that triggered each sweep is shown only for the first condition; scale bar indicates current injection. The second trace (Normal) is the recording from the postsynaptic target in physiological saline. The third trace (20/20) is the recording in 20 mM Ca^{2+} / 20 mM Mg^{2+} saline to block polysynaptic transmission. The fourth trace (0/20) is in 0 mM Ca^{2+} / 20 mM Mg^{2+} saline to block all transmission. The bottom trace (Wash) is again in normal saline.

and the reference drive signal as $U(t)$. The spectral coherence was defined as follows:

$$C_i(f) = \frac{\frac{1}{K}\sum_{k=1}^{K} \tilde{V}_i^{(k)}(f)\left[\tilde{U}^{(k)}(f)\right]^*}{\sqrt{\left(\frac{1}{K}\sum_{k=1}^{K}\left|\tilde{V}_i^{(k)}(f)\right|^2\right)\left(\frac{1}{K}\sum_{k=1}^{K}\left|\tilde{U}^{(k)}(f)\right|^2\right)}}.$$

To calculate the standard errors for the coherence estimates, we again used the jackknife (Thomson and Chave, 1991) and computed delete-one averages of coherence, denoted $C_n^{(k)}(f)$, where n is the index of the deleted taper:

$$C_i^{(n)}(f) = \frac{\frac{1}{K-1}\sum_{\substack{k=1\\k\neq n}}^{K} \tilde{V}_i^{(k)}(f)\left[\tilde{U}^{(k)}(f)\right]^*}{\sqrt{\left(\frac{1}{K-1}\sum_{\substack{k=1\\k\neq n}}^{K}\left|\tilde{V}_i^{(k)}(f)\right|^2\right)\left(\frac{1}{K-1}\sum_{\substack{k=1\\k\neq n}}^{K}\left|\tilde{U}^{(k)}(f)\right|^2\right)}}.$$

Estimating the standard error of the magnitude of $C_i(f)$ requires an extra step, similar to the case for the spectral power, since $|C_i(f)|$ is defined on the interval [0, 1] while Gaussian variables exist on $(-\infty, \infty)$. The delete-one estimates, $|C_i^{(n)}(f)|$, were replaced with the following transformed values:

$$g\{|C_i|\} = ln\left(\frac{|C_i|^2}{1-|C_i|^2}\right)$$

or

$$|C_i| = \frac{1}{\sqrt{1+e^{-g\{|C_i|\}}}}.$$

The mean of the transformed variable is as follows:

$$\mu_{i;\,Mag}(f) = \frac{1}{K}\sum_{n=1}^{K} g\left\{C_i^{(n)}(f)\right\}$$

NOTES

and standard error of the transformed variable is as follows:

$$\sigma_{i;\,\mathrm{Mag}}(f) = \sqrt{\frac{K-1}{K}\sum_{n=1}^{K}\left|g\left\{C_i^{(n)}(f)\right\} - \mu_{i;\,\mathrm{Mag}}(f)\right|^2}\,.$$

The 95% confidence interval for the coherence is

$$\left[\sqrt{1+e^{-(\mu_{i;\mathrm{Mag}}-2\sigma_{i;\mathrm{Mag}})}}^{-1},\ \sqrt{1+e^{-(\mu_{i;\mathrm{Mag}}+2\sigma_{i;\mathrm{Mag}})}}^{-1}\right].$$ For

completeness, an alternate transformation for computing the variance is $g\{|C_i|\} = tanh^{-1}\{|C_i|\}$.

We now consider an estimate of the standard deviation of the phase of $C(f)$. Conceptually, the idea is to compute the variation in the relative directions of the delete-one unit vectors $C_i(f)/|C_i(f)|$. The standard error is computed as follows:

$$\sigma_{i;\,\mathrm{Phase}}(f) = \sqrt{2\,\frac{K-1}{K}\left(K - \left|\sum_{n=1}^{K}\frac{C_i^{(n)}(f)}{\left|C_i^{(n)}(f)\right|}\right|\right)}\,.$$

Our interest lies in the values of $C_i(f)$ for $f = f_{Drive}$ and the confidence limits for these values. We chose the bandwidth so that the estimate of $|C_i(f_{Drive})|$ is kept separate from that of the harmonic $|C_i(2f_{Drive})|$; the choice $\Delta f = 0.4\, f_{Drive}$ works well. We thus graph the magnitude and phase of $C_i(f_{Drive})$ for all neurons, along with the confidence interval, on a polar plot (Fig. 2*E*).

Finally, we consider whether the coherence of a given cell at f_{Drive} is significantly greater than zero, that is, larger than one would expect to occur by chance from a signal with no coherence, as a means of selecting candidate postsynaptic targets of Tr2. We compared the estimate for each value of $|C_i(f_{Drive})|$ to the null distribution for the magnitude of the coherence, which exceeds

$$\left|C_i(f_{\mathrm{Drive}})\right| = \sqrt{1-\alpha^{1/(K-1)}}$$

only in α of the trials (Hannan, 1970; Jarvis and Mitra, 2001). We used $\alpha = 0.001$ in our experiments to avoid false-positives. We also calculated the multiple comparisons of α level for each trial, given by $\alpha_{multi} = 1 - (1-\alpha)^N$, where N is the number of cells in the functional image, and verified that it did not exceed $\alpha_{multi} = 0.05$ on any trial.

The result of the above procedure was the discovery of three postsynaptic targets of cell Tr2, two of which were functionally unidentified neurons (Taylor et al., 2003) (Fig. 2*F*).

Case three

Rats can palpate objects via highly regular rhythmic whisking (Berg and Kleinfeld, 2003). Motivated by ideas from control theory, we conjectured that primary motor (M1) cortex transforms sensory input to serve as a feedback signal for the smooth motion of the vibrissae. We posed the question of whether a punctate periodic input (such as occurs when the animal rhythmically palpates an object) is transformed into a pure sinusoidal signal over the 5-20 Hz range of normal whisking frequencies.

To test this theory, we had awake rats hold their vibrissae still as periodic air puffs were delivered. Records from primary sensory cortex (S1) showed a known punctate response, while those from M1 were smooth (Figs. 3*A*,*E*). The stimulus-driven power spectrum for the S1 unit displayed multiple harmonics (Fig. 3*B*) consistent with a pulsatile response, while that for the M1 unit appeared to have power only at the fundamental frequency of the stimulus repetition rate, denoted f_1 (Fig. 3*F*). We consequently asked whether the motor response could be replaced with a pure sinusoidal process with a frequency of f_1. Thus, the time series for the spike rate must take the following form:

$$V(t) = A_1\, cos(2\pi f_1 t + \varphi_1) + \eta(t)\,,$$

where $\eta(t)$ is the residual noise. We recall that $cos(x) = \tfrac{1}{2}(e^{ix} + e^{-ix})$ and define

$$B_1 \equiv \frac{A_1}{2}\, e^{i\varphi_1}$$

so that $V(t)$ can be placed in a computationally convenient form, as follows:

$$V(t) = B_1\, e^{i\,2\pi f_1 t} + B_1^*\, e^{-i\,2\pi f_1 t} + \eta(t).$$

As a means of estimating the complex amplitude B_1, we first make multiple estimates of the spectra in the

NOTES

vicinity of frequency f_1 so that we can regress over a number of tapers to determine B_1. The Fourier transform of $V(t)$ with respect to the kth taper is as follows:

$$\tilde{V}^{(k)}(f) = \frac{B_1}{\sqrt{T}} \int_0^T dt\ e^{-i2\pi f t} w^{(k)}(t) e^{i2\pi f_1 t} + \frac{B_1^*}{\sqrt{T}} \int_0^T dt\ e^{-i2\pi f t} w^{(k)}(t) e^{-i2\pi f_1 t} + \frac{1}{\sqrt{T}} \int_0^T dt\, e^{-i2\pi f t} w^{(k)}(t)\, \eta(t).$$

This compresses to

$$\tilde{V}^{(k)}(f) = B_1\, \tilde{w}^{(k)}(f - f_1) + B_1^*\, \tilde{w}^{(k)}(f + f_1) + \tilde{\eta}^{(k)}(f)\ ,$$

where we defined the spectrum of the kth taper as

$$\tilde{w}^{(k)}(f) = \frac{1}{\sqrt{T}} \int_0^T dt\ e^{-i2\pi f t}\ w^{(k)}(t)$$

and the kth spectral estimate of the residual as

$$\tilde{\eta}^{(k)}(f) = \frac{1}{\sqrt{T}} \int_0^T dt\ e^{-i2\pi f t}\ w^{(k)}(t)\, \eta(t)\ .$$

The estimate of the transform at the frequency of interest, $f = f_1$, becomes

$$\tilde{V}^{(k)}(f_1) = \begin{cases} B_1 \tilde{w}^{(k)}(0) + \tilde{\eta}^{(k)}(f_1) & \text{for } k = 1, 3, 5, \ldots \\ \tilde{\eta}^{(k)}(f_1) & \text{for } k = 2, 4, 6, \ldots \end{cases}$$

where we used $\tilde{w}^{(k)}(2f_1) = 0$ from the condition $2f_1 > \Delta f$, i.e., the spectrum of a taper has no amplitude outside of its bandwidth, and note that $w^{(k)}(t)$ is an odd function for even values of k.

The above relation specifies a regression for B_1 over odd values of k, where the $\tilde{V}^{(k)}(f_1)$ are the dependent variables and the $\tilde{\eta}^{(k)}(f_1)$ are the independent variables. The least-squares estimate of B_1, denoted $\hat{B}_1$, is as follows:

$$\hat{B}_1 = \frac{\sum_{k = 1, 3, 5, \ldots}^{K} \tilde{w}^{(k)}(0)\ \tilde{V}^{(k)}(f_1)}{\sum_{k = 1, 3, 5, \ldots}^{K} \left[\tilde{w}^{(k)}(0)\right]^2}$$

and the associated F-statistic is derived to be the following (Thomson, 1982):

$$F_{2,\,2K-2} = \left|\hat{B}_1\right|^2 \frac{(K-1) \sum_{k=1}^{K} \left|\tilde{w}^{(k)}(0)\right|^2}{\sum_{k=1}^{K} \left|\tilde{V}^{(k)}(f_1) - \hat{V}^{(k)}(f_1)\right|^2}$$

The formula below is the estimated contribution of the periodic signal to the continuous spectrum:

$$\hat{V}^{(k)}(f_1) = \begin{cases} \hat{B}_1 \tilde{w}^{(k)}(0) & \text{for } k = 1, 3, 5, \ldots \\ 0 & \text{for } k = 2, 4, 6, \ldots \end{cases}$$

NOTES

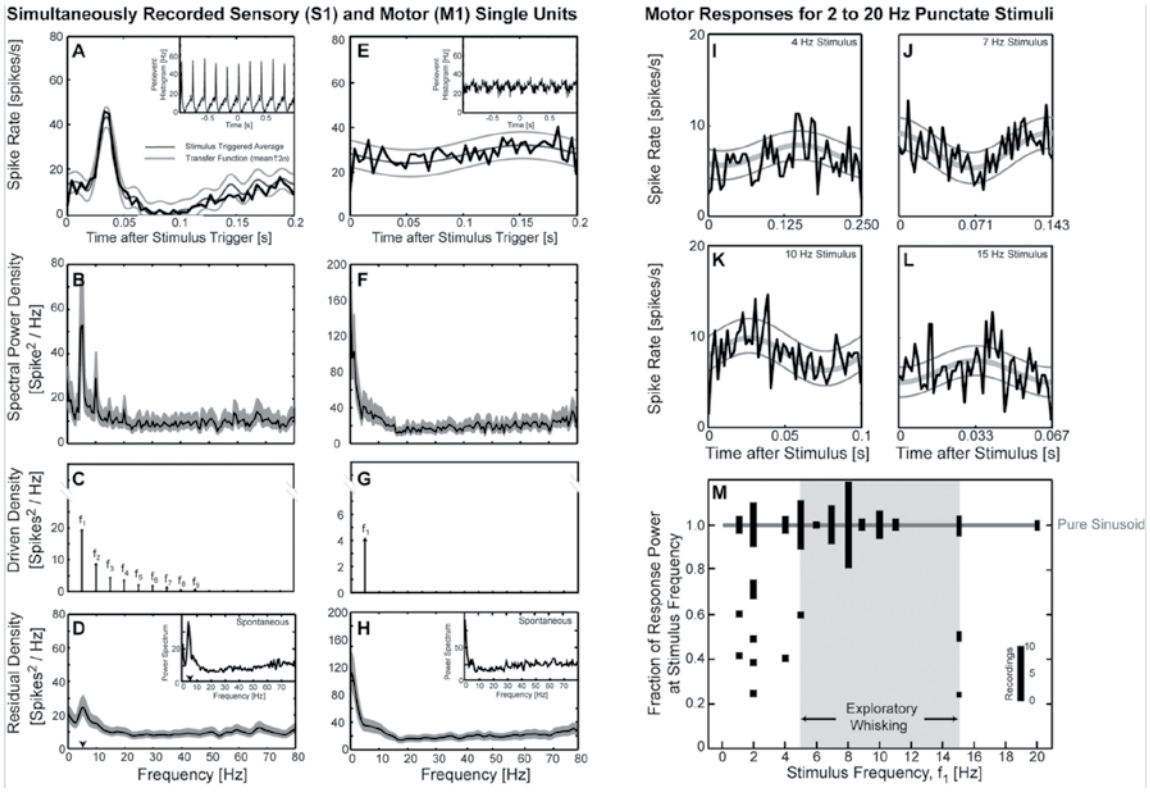

Figure 3. Simulated analysis of single unit data from S1 and M1 cortices as a single vibrissa of an awake but immobile rat (Kleinfeld et al., 2002, their Fig. 3 and Fig. 5, reprinted with permission from Neuron). ***A, E,*** Stimulus-triggered average and transfer function between the stimulus and the instantaneous spike rate of sensory and motor units (thin black line) for vibrissa stimulation at 5 Hz. The transfer function was computed from a spectral decomposition (T = 100 s; K = 99) of the time series of the response. ***B***, ***F***, Spectral power of the unit spike response; full bandwidth Δf = 1.0 Hz. ***C***, ***G***, The spectral power for the stimulus-driven part of the response. The height of each arrow corresponds to the magnitude of the complex coefficient for power at the fundamental frequency of the stimulus, denoted f_1, or at the nth harmonic of the stimulus, f_n. Only coefficients that surpassed the value set by an F-test were accepted and used to reconstruct the transfer functions in panels *A* and *E*, respectively. ***D***, ***H***, Power for the residual response, found by subtracting the stimulus driven components in the power (panels *C* and *G*) from the spectrum (panels *B* and *F*). For the S1 unit, note the excess power near 5 Hz (arrow in panel *D*) that is also present in the spontaneous activity. Note, too, the presence of low-frequency spiking in the residual activity for the M1 unit as well as in the spontaneous activity. ***I–L***, Summary results from a unit to show the peristimulus time histogram (black curve) and the best fit (gray curve) at four different stimulation frequencies: 4, 7, 10, and 15 Hz; at all four frequencies, the modulated spike rate captures only the fundamental frequency of the stimulus. ***M***, Summary of the relative power at f_1 for all motor units in the study. A value of 1 indicates that the unit follows only the fundamental frequency of the stimulus. The height of a bar corresponds to the number of separate units. Panels ***A, B, D, E, F, H, I, J, K***, and ***L*** plot the mean and two standard error limits.

We accept the estimator $\hat{B}_l$ if the F-statistic exceeds $1 - 1/N_t$, where N_t is the number of points in $V(t)$. If $\hat{B}_l$ is significant, we move to another frequency in order to determine the complete set of estimators, denoted $\hat{B}_m$ with $m = 1, \ldots, M$, for all M sinusoidal components. The final spectrum is expressed below:

$$S(f) = \sum_{m=1}^{M}\left[\frac{1}{K}\sum_{k=1}^{K}\left|\tilde{V}^{(k)}(f) - \hat{B}_m\tilde{w}^{(k)}\left(f - f_m\right)\right|^2 + \left|\hat{B}_m\right|^2\delta\left(f - f_m\right)\right].$$

This is shown for the example M1 and S1 units (Figs. 3*C*,*D*,*G*,*H*); the same expansion coefficients are used to construct transfer functions for the response (Figs. 3*A*,*E*). Note the low-frequency peak in the residual spiking activity for both units that matches the respective spontaneous activity (Figs. 3*D*,*H*). Finally, a

NOTES

measure of the purity of pitch determination is given by the ratio of the power at the fundamental to the total power:

$$\hat{C}(f_1) = \frac{\left|\hat{B}(f_1)\right|^2}{\sum_{m=1}^{M}\left|\hat{B}(mf_1)\right|^2}.$$

Of interest, the above measure was found to be $\hat{C}(f_1)=1$ only when the vibrissa stimulation was between 5 Hz and 20 Hz (Fig. 3M)—the natural whisking frequencies. Linear filtering cannot explain such an effect, and it was conjectured that an active filtering process, such as the neurological realization of a phase-locked loop, underlies this process (Kleinfeld et al., 2002).

Case four

A common issue that arises in the analysis of optical imaging data is to remove "fast" noise—that is, fluctuations in intensity that occur on a pixel-by-pixel and frame-by-frame basis. The idea is that the imaging data contain features that are highly correlated in space, such as underlying cell bodies and processes, and highly correlated in time, such as long-lasting responses. The imaging data may thus be viewed as a space-time matrix of random numbers: i.e., the fast noise, with added correlated structure.

With this model in mind, we focus on the case of Ca^{2+} waves in an organotypic culture of rat cortex, which contains both neurons and glia. All cells were loaded with a calcium indicator, and spontaneous activity in the preparation was imaged using a fast-framing (f_{sample} = 500 Hz), low-resolution (100 × 100 pixels) confocal microscope (Fig. 4*A*).

Imaging data takes the form of a three-dimensional array of intensities, denoted $V(x, y, t)$. We consider expressing the spatial location in terms of a pixel index so that each $(x, y) \rightarrow s$ and the data are now in the form of a space-time matrix $V(s, t)$. This matrix may be decomposed into the outer product of functions of pixel index and functions of time. Specifically,

$$V(s,t) = \sum_{n=1}^{rank\{V\}} \lambda_n F_n(s)\, G_n(t),$$

where the rank of $V(s, t)$ is the smaller of the pixel or time dimensions. For example data (Fig. 4*A*), there are N_t = 1200 frames, or time points, and N_s = 10,000 pixels, so that $rank\{V(s, t)\} = N_t$. The above decomposition is referred to as an SVD (Golub and Kahan, 1965). The temporal functions satisfy this eigenvalue equation:,

$$\sum_{t'=1}^{N_t} G_n(t') \left[\sum_{s=1}^{N_s} V(s,t)V(s,t')\right] = \lambda_n^2 G_n(t),$$

where the functions $F_n(s)$ and $G_n(t)$ are orthonormal, so that

$$\sum_{t=1}^{N_t} G_m(t)\, G_n(t) = \delta_{nm}$$

and

$$\sum_{s=1}^{N_s} F_m(s)\, F_n(s) = \delta_{nm}.$$

The spatial function that accompanies each temporal function is found by inverting the defining equation, so that the following holds true:

$$F_n(s) = \frac{1}{\lambda_n}\sum_{t=1}^{N_t} V(s,t)\, G_n(t).$$

When this decomposition is applied to the Ca^{2+} imaging data (Fig. 4*A*), we see that the eigenvalue spectrum has some very large values for the low-order modes but then rapidly falls to a smoothly decreasing function of index (Fig. 5*A*). (Theoretical

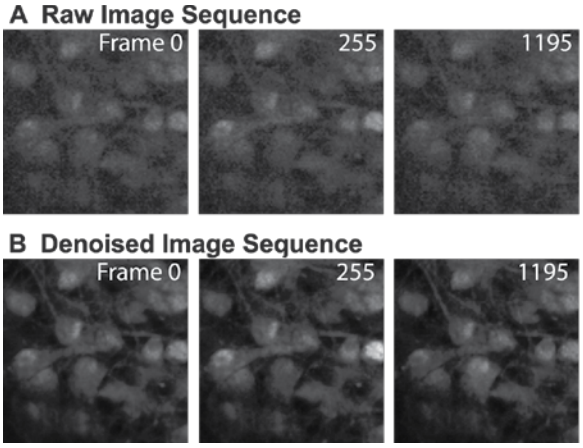

Figure 4. Denoising of spinning-disk confocal imaging data on Ca^{2+} waves in organotypic culture. ***A***, Selected frames from a 1200-frame sequence of 100 × 100 pixel data. ***B***, The same data set after reconstruction with 25 of the 1200 modes. Denoising is particularly clear when the data are viewed as video clips.

NOTES

expressions for the baseline distribution may be found in Sengupta and Mitra, 1999.) The spatial and temporal modes show defined structure for the first 15 modes; beyond these, the spatial modes appear increasingly grainy, and the temporal modes appear as fast noise (Figs. 5*B*,*C*).

The utility of this decomposition is that only the lower-order modes carry information. Thus, we can reconstruct the data matrix from only these modes and remove the "fast" noise, as follows:

$$V^{\text{reconstructed}}(s, t) = \sum_{n=1}^{\text{largest signficant mode}} \lambda_n F_n(s) G_n(t).$$

Compared with smoothing techniques, the truncated reconstruction respects all correlated features in the data and, for example, does not remove sharp edges. Reconstruction of the Ca^{2+}-wave data highlights the correlated activity by removing fast, grainy-looking variability (Fig. 4*B*).

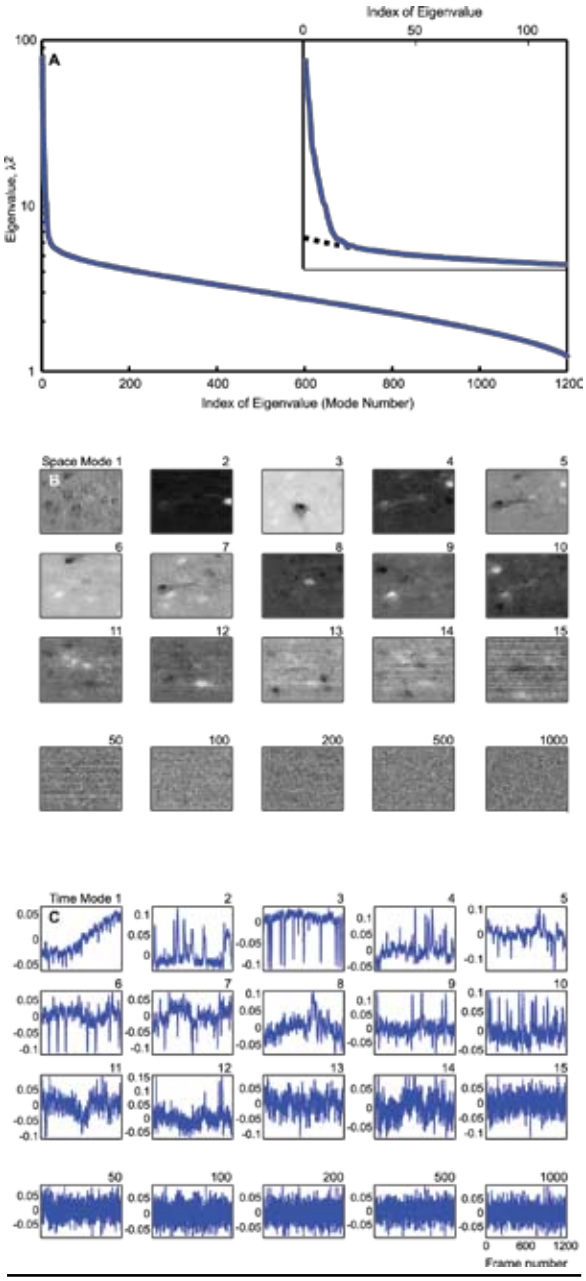

Figure 5. SVD of the imaging sequence in Figure 4. ***A***, The spectrum for the square of the eigenvalues for the space and time modes. Note the excess variance in the roughly 25 dominant modes. ***B***, Top 15 spatial modes, $F_n(s)$, plus high-order modes. ***C***, Top temporal modes, $G_n(t)$.

Case five

The final example concerns the characterization of coherent spatiotemporal dynamics. We return to the use of voltage-sensitive dyes, this time to image the electrical dynamics of turtle visual cortex in response to a looming stimulus. Early work had shown that a looming stimulus led to the onset of ~20 Hz oscillations, the γ-band for turtle, in visual cortex. The limited range of cortical connections suggested this oscillation might be part of wave motion. Yet the raw data, even after denoising and broadband filtering, appears complex (Fig. 5*A*): Regions of net depolarization sweep across cortex, but no simple pattern emerges.

One possible explanation is that cortex supports multiple dynamic processes, each with a unique center frequency, that may be decomposed by an SVD in the frequency domain. In this method (Mann and Park, 1994), the space-time data $V(s, t)$ are first projected into a local temporal frequency domain by transforming them with respect to a set of tapers:

$$\tilde{V}^{(k)}(s, f) = \frac{1}{\sqrt{T}} \int_0^T dt\, e^{i 2\pi f t}\, w^{(k)}(t)\, V(s,t).$$

The index k defines a local frequency index in the band $[f - \Delta f/2, f + \Delta f/2]$. For a fixed frequency, f_0, an SVD is performed on this complex matrix:

$$\tilde{V}(s, k; f_0) \equiv \left[\tilde{V}^{(1)}(s, f_0), \ldots, \tilde{V}^{(K)}(s, f_0)\right].$$

This yields the following:

$$\tilde{V}(s, k; f_0) = \sum_{n=1}^{\text{rank}\{\tilde{V}\}} \lambda_n \tilde{F}_n(s) \tilde{G}_n(k),$$

NOTES

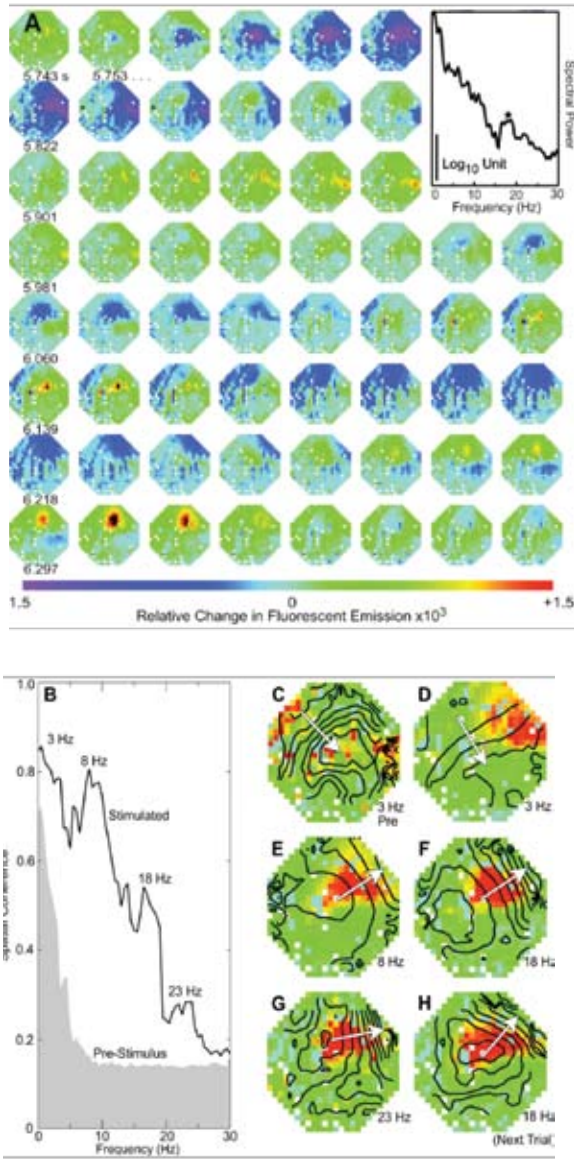

Figure 6. Analysis of single-trial, voltage-sensitive dye imaging data to delineate collective excitation in visual cortex of turtle (Prechtl et al., 1997, their Fig. 2 and Fig. 3, reprinted with permission from Proceedings of the National Academy of Sciences USA). ***A***, Response while the animal was presented with a looming stimulus. The data were denoised, low-pass filtered at 60 Hz, and median filtered (400 ms width) to remove a stimulus-induced depolarization. We show every eighth frame (126 Hz); note the flow of depolarization from left to right. Insert is the spectrum for the interval 4.7 to 5.7 s ***B***, Coherence, $\hat{C}(f_0)$, over intervals both before and after the onset of the stimulus (T = 3 s; K = 7) estimated at successive frequency bins; $C(f) > 0.14$ indicates significance. ***C***, Spatial distribution of amplitude (red for maximum and blue for zero) and phase ($\pi/12$ radians per contour; arrow indicates dominant gradient) of the coherence at f = 3 Hz prior to stimulation. ***D–G***, Amplitude and phase at f = 3, 8, 18, and 22 Hz during stimulation. ***H***, Amplitude and phase at 18 Hz for the next trial (compare panels *F* and *H*).

where the rank is invariably set by K. A measure of coherence is given by the ratio of the power of the leading mode to the total power (Fig. 6*B*):

$$\hat{C}(f_0) = \frac{\lambda_1^2(f_0)}{\sum_{k=1}^{K} \lambda_k^2(f_0)}.$$

A completely coherent response leads to $\hat{C}(f_0) = 1$, while for a uniform random process $\hat{C}(f_0) = 1/K$. Where $\hat{C}(f_0)$ has a peak, it is useful to examine the largest spatial mode, $\tilde{F}_1(s)$. The magnitude of this complex image gives the spatial distribution of coherence at f_0, while gradients in its phase indicate the local direction of propagation.

For the example data (Fig. 6*A*), this analysis revealed linear waves as the dominant mode of electrical activity; those at 3 Hz were present with or without stimulation while those at 8 through 23 Hz were seen only with stimulation and propagate orthogonal to the wave at 3 Hz (Figs. 6*C*, *H*). It is of biological interest that the waves at 3 Hz track the direction of thalamocortical input, while those at higher frequencies track a slight bias in axonal orientation (Cosans and Ulinski, 1990) that was unappreciated in the original work (Prechtl et al., 1997).

References

Berg RW, Kleinfeld D (2003) Rhythmic whisking by rat: Retraction as well as protraction of the vibrissae is under active muscular control. J Neurophysiol 89:104-117.

Cacciatore TW, Brodfueher PD, Gonzalez JE, Jiang T, Adams SR, Tsien RY, Kristan Jr. WB, Kleinfeld D (1999) Identification of neural circuits by imaging coherent electrical activity with FRET-based dyes. Neuron 23:449-459.

Cosans CE, Ulinski PS (1990) Spatial organization of axons in turtle visual cortex: Intralamellar and interlamellar projections. J Comp Neurol 296:548-558.

Drew PJ, Duyn JH, Galanov E, Kleinfeld D (2008) Finding coherence in spontaneous oscillations. Nat Neurosci 11:991-993.

Golub GH, Kahan W (1965) Calculating singular values and pseudo-inverse of a matrix. Philadelphia: Society for Industrial and Applied Mathematics.

Hannan EJ (1970) Multiple time series. New York, NY: Wiley.

Jarvis MR, Mitra PP (2001) Sampling properties of the spectrum and coherency of sequences of action potentials. Neural Comp 13:717-749.

Kleinfeld D, Sachdev RNS, Merchant LM, Jarvis MR, Ebner FF (2002) Adaptive filtering of vibrissa input in motor cortex of rat. Neuron 34:1021-1034.

Mann ME, Park J (1994) Global-scale modes of surface temperature variability on interannual to centuries timescales. J Geophys Res 99:25819-25833.

Mitra PP, Bokil HS (2008) Observed brain dynamics. New York: Oxford UP.

Mitra PP, Pesaran B (1998) Analysis of dynamic brain imaging data. Biophys J 76:691-708.

Mitra PP, Pesaran B, Kleinfeld D (1999) Analysis of dynamic optical imaging data. In: Imaging: a laboratory manual (Yuste R, Lanni F, Konnerth A, eds). Cold Spring Harbor, NY: Cold Spring Harbor Laboratory Press.

Nir Y, Mukamel R, Dinstein I, Privman E, Harel M, Fisch L, Gelbard-Sagiv H, Kipervasser S, Andelman F, Neufeld MY, Kramer U, Arieli A, Fried I, Malach R (2008) Interhemispheric correlations of slow spontaneous neuronal fluctuations revealed in human sensory cortex. Nat Neurosci 11:1100–1108.

Percival DB, Walden AT (1993) Spectral analysis for physical applications: multitaper and conventional univariate techniques. Cambridge: Cambridge UP.

Prechtl JC, Cohen LB, Mitra PP, Pesaran B, Kleinfeld D (1997) Visual stimuli induce waves of electrical activity in turtle cortex. Proc Natl Acad Sci USA 94:7621-7626.

Sengupta AM, Mitra PP (1999) Distributions of singular values for some random matrices. Phys Rev E Stat Phys Plasmas Fluids Relat Interdiscip Topics 60:3389-3392.

Taylor AL, Cottrell GW, Kleinfeld D, Kristan WB (2003) Imaging reveals synaptic targets of a swim-terminating neuron in the leech CNS. J Neurosci 23:11402–11410.

Thomson DJ (1982) Spectral estimation and harmonic analysis. Proc IEEE 70:1055-1096.

Thomson DJ, Chave AD (1991) Jackknifed error estimates for spectra, coherences, and transfer functions. In: Advances in spectrum analysis and array processing (Haykin S, ed), pp 58-113. Upper Saddle River, NJ: Prentice Hall.

NOTES